



Cite this: *Chem. Commun.*, 2015, 51, 2609

Received 5th December 2014,  
Accepted 24th December 2014

DOI: 10.1039/c4cc09725d

www.rsc.org/chemcomm

## Catalyst-loaded porous WO<sub>3</sub> nanofibers using catalyst-decorated polystyrene colloid templates for detection of biomarker molecules†

Seon-Jin Choi, Sang-Joon Kim, Won-Tae Koo, Hee-Jin Cho and Il-Doo Kim\*

**Pore-loaded WO<sub>3</sub> nanofibers (NFs) functionalized with spherical catalyst films were achieved via electrospinning combined by the sacrificial templating route using layer-by-layer (LbL) catalyst assembled polystyrene (PS) colloids. The catalyst-loaded porous WO<sub>3</sub> NFs exhibited significantly improved toluene and acetone detection capability for potential application in exhaled breath analysis.**

Breath analysis is receiving great attention for non-invasive diagnosis of diseases and daily health monitoring. A number of breath biomarkers such as toluene (C<sub>6</sub>H<sub>5</sub>CH<sub>3</sub>), acetone (CH<sub>3</sub>COCH<sub>3</sub>), carbon monoxide (CO), nitrogen monoxide (NO), and hydrogen sulfide (H<sub>2</sub>S) have been identified for diagnosis of lung cancer,<sup>1,2</sup> diabetes,<sup>3</sup> chronic obstructive pulmonary disease (COPD),<sup>4</sup> asthma,<sup>5</sup> and halitosis,<sup>6</sup> respectively. These components are exhaled through breath with concentrations ranging from parts per billion (ppb) to sub-parts per million (ppm) levels. Generally, patient breath contains higher concentrations of biomarker molecules compared to the concentrations in the breath of healthy people. For example, toluene concentration is increased to 10–100 ppb in the breath of lung cancer patients compared to that (1–20 ppb) of healthy people.<sup>2,7</sup> Several promising studies demonstrated the potential diagnosis of lung cancer using breath analysis,<sup>8,9</sup> exhibiting the critical advantages of a non-invasive screening method compared to the conventional invasive screening techniques such as computed tomography and bronchoscopy.

Recently, semiconducting metal oxide (SMO)-based sensing layers have received intensive attention for potential application in the early diagnosis of diseases by breath analysis due to the low cost for preparation, simple operating principles, and capability of portable use with real-time diagnosis.<sup>10</sup> To achieve highly sensitive detection of sub-ppm level breath molecules,

a high surface-to-volume ratio and large porosity are essential for SMO-based sensors, considering that the reaction occurs on the surface. In addition, catalytic functionalization of noble metallic nanoparticles should be indispensably accompanied for selective detection of SMO-based sensors. Thus far, a number of promising results have demonstrated the potential analysis of breath biomarkers such as H<sub>2</sub>S and acetone for diagnosis of halitosis and diabetes using Au–SnO<sub>2</sub> hollow spheres,<sup>11</sup> Si-doped WO<sub>3</sub> nanoparticles,<sup>12</sup> and graphene–WO<sub>3</sub> hemitubes,<sup>13</sup> which showed high porosity as well as catalytic activity, thereby exhibiting remarkable sensitivity and selectivity.

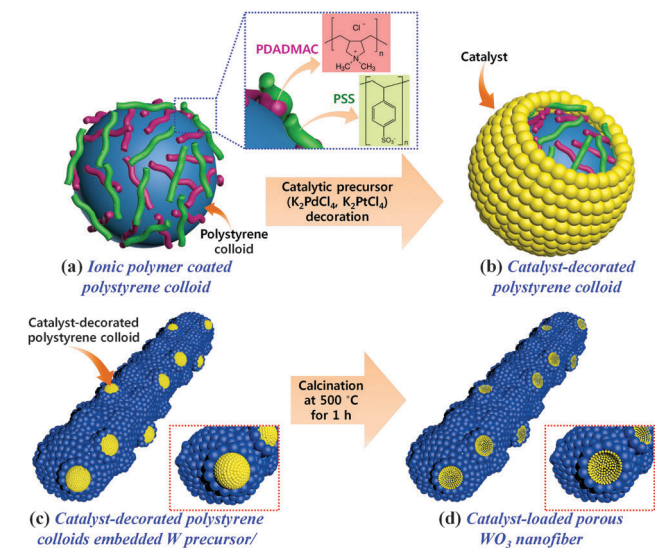
Electrospinning has been distinguished as an effective synthetic method to produce one-dimensional (1D) nanofibrous structures with high porosity.<sup>14,15</sup> For example, highly porous non-woven structures of NiO<sup>16</sup> and ZnO nanotubes<sup>17</sup> were demonstrated using electrospinning. In addition, several catalyst functionalizations on SMO nanofibers (NFs) have been proposed. They include the simple mixing between polyol-synthesized catalytic nanoparticles and electrospun SMO NFs, as well as solution electrospinning including catalytic precursors. Pt–SnO<sub>2</sub> NFs,<sup>18</sup> Pd–SnO<sub>2</sub> NFs,<sup>19</sup> and Pd–WO<sub>3</sub> NFs<sup>20</sup> are examples of catalyst-decorated SMO NF composite sensing layers. However, catalytic functionalization of pore-loaded SMO NFs using metallic films coated on spherical colloids has never been reported.

In this work, we propose a new catalyst functionalization method for selectively embedding thin-walled catalysts, which are formed at the pore sites, in electrospun metal oxide NFs. Catalyst-decorated polystyrene (PS) colloid templates assisted by layer-by-layer (LbL) assembly<sup>21,22</sup> were utilized to uniformly functionalize catalytic particles and generate pores on electrospun SMO NFs. Firstly, PS colloids were coated by ionic polymers, *i.e.*, cationic poly(diallyldimethylammonium chloride) (PDADMAC) and anionic poly(styrenesulfonate) (PSS), to form PDADMAC/PSS/PDADMAC multi-stacked layers (Scheme 1a). Then, catalytic precursors such as K<sub>2</sub>PdCl<sub>4</sub> and K<sub>2</sub>PtCl<sub>4</sub> were decorated on the ionic polymer-coated PS colloids (Scheme 1b). The synthesized catalyst-decorated PS colloids were introduced in electrospinning solution to form catalyst-decorated PS colloid-embedded

Department of Materials Science and Engineering, Korea Advanced Institute of Science and Technology (KAIST), Daejeon 305–701, Republic of Korea.

E-mail: idkim@kaist.ac.kr; Fax: +82-42-350-5329; Tel: +82-42-350-3329

† Electronic supplementary information (ESI) available: Experimental details, energy dispersive X-ray spectroscopy (EDS) analysis, exponential approximation of detection limit, pore distribution analysis, and additional sensing performances of Pd-loaded porous WO<sub>3</sub> NFs. See DOI: 10.1039/c4cc09725d



**Scheme 1** Schematic illustration of the synthesis process for catalyst-loaded porous  $\text{WO}_3$  nanofibers (NFs) assisted by catalyst-decorated colloid templates: (a) cationic and anionic polymer-coated polystyrene (PS) colloid, (b) catalyst-decorated PS colloid template, (c) catalyst-decorated PS colloid templates embedded as-spun W precursor-PVP composite NF, and (d) catalyst-loaded porous  $\text{WO}_3$  NF after calcination at  $500^\circ\text{C}$  for 1 h.

W precursor-poly(vinylpyrrolidone) (PVP) composite NFs (Scheme 1c). Finally, catalyst-loaded  $\text{WO}_3$  NFs having spherical or crater-like shape pores with size distribution ranging 200–300 nm were achieved after calcination at  $500^\circ\text{C}$  for 1 h (Scheme 1d).

Fig. 1 presents morphological and structural observations of catalyst-decorated PS colloid templates and locally Pd-loaded porous  $\text{WO}_3$  NFs. Spherical structures of pristine PS colloids having an average diameter of 500 nm exhibited smooth surface morphology before catalyst decoration (Fig. 1a). The catalytic precursor of  $\text{K}_2\text{PdCl}_4$  was coated on the PS colloid surface modified by LbL assembly of the ionic PDADMAC/PSS/PDADMAC multilayer (see ESI<sup>†</sup>), which resulted in a rough surface of PS colloids (hereafter, Pd-decorated PS colloids referred to as Pd-PS colloids) (Fig. 1b). Energy-dispersive X-ray spectroscopy (EDS) analysis revealed the assembled Pd catalysts on the surface of PS colloids (see ESI<sup>†</sup>, Fig. S1). The synthesized Pd-PS colloids were introduced in electrospinning solution, which results in well-distributed Pd-PS colloids (white arrows) embedded W precursor-PVP composite NFs (Fig. 1c). The Pd-PS colloids were converted into pores after calcination at  $500^\circ\text{C}$  for 1 h, leaving catalytic Pd particles at the pore sites (Fig. 1d and e) (see ESI<sup>†</sup>). To confirm the Pd particles after calcination, EDS analysis using SEM was performed, which reveals the functionalization of Pd at the open pore sites (see ESI<sup>†</sup>, Fig. S2). Different types of pore structures were formed after the calcination, e.g. closed pores exhibiting an extruded structure and open pores exhibiting a crater-like structure on the surface of  $\text{WO}_3$  NFs (Fig. 1e), which were attributed to the decomposition of the randomly distributed PS colloid templates within the W precursor-PVP composite NFs. The detailed pore structure as well as crystallographic structure of Pd-loaded porous  $\text{WO}_3$  NFs were identified by TEM analysis (Fig. 1f–i). TEM analysis

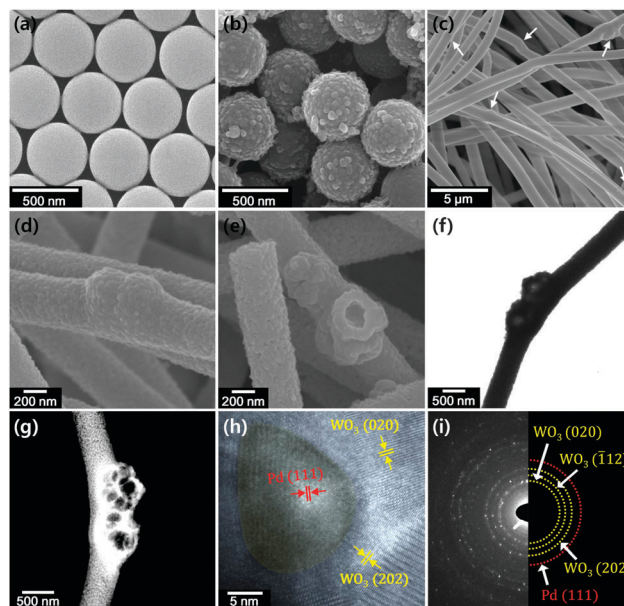


**Fig. 1** Morphological and structural observation of Pd-loaded porous electrospun  $\text{WO}_3$  nanofibers (NFs) assisted by Pd-decorated polystyrene (PS) colloid templates in electrospinning: SEM images of (a) PS colloid templates, (b) Pd-decorated PS colloids using layer-by-layer (LbL) assembly, (c) as-spun W precursor-PVP composite NFs containing Pd-decorated PS colloids, (d) Pd-loaded  $\text{WO}_3$  NFs after calcination at  $500^\circ\text{C}$  for 1 h, and (e) magnified SEM image of (d) at open pores. (f) TEM image, (g) scanning TEM (STEM) image, (h) high-resolution (HR) TEM image, and (i) selected area electron diffraction (SAED) pattern of Pd-loaded porous  $\text{WO}_3$  NF.

revealed that dense  $\text{WO}_3$  NFs contain multiple pores on the surface (Fig. 1f). Scanning TEM (STEM) analysis also demonstrated that the aggregated pores were observed on the surface of  $\text{WO}_3$  NFs, which was attributed to the decomposition of the aggregated Pd-PS colloid templates (Fig. 1g). The high-resolution TEM (HRTEM) analysis illustrated highly crystallized  $\text{WO}_3$  and Pd that exhibited crystal planes of  $\text{WO}_3(020)$ ,  $\text{WO}_3(202)$ , and  $\text{Pd}(111)$ , which correspond to interplanar distances of 3.7 Å, 2.6 Å, and 2.3 Å, respectively (Fig. 1h). Selected area electron diffraction (SAED) pattern analysis revealed the polycrystalline characteristic of  $\text{WO}_3$  NFs exhibiting crystal planes of (020), ( $\bar{1}12$ ), and (202) (Fig. 1i), which were partially identified in HRTEM analysis. In addition, a blur electron diffraction pattern of Pd was observed with the crystal plane of (111), corresponding to an interplanar distance of 2.3 Å (Fig. 1i). For further confirmation of Pd particles, EDS elemental mapping analysis using TEM was performed so that concentrated Pd decoration was observed at the pore sites (see ESI<sup>†</sup>, Fig. S3). The minor Pd-decorated spots across the  $\text{WO}_3$  NFs in the EDS mapping image were attributed to the detached Pd particles from the Pd-PS colloid templates during the vigorous stirring in the preparation of the electrospinning solution. The obtained pore structures as well as catalyst decoration can enhance gas sensing performance by facilitating gas penetration and the catalytic effect.<sup>23</sup>

The gas sensing performances of dense  $\text{WO}_3$  NFs, porous  $\text{WO}_3$  NFs synthesized by PS colloid templates without Pd decoration (referred to as PS- $\text{WO}_3$  NFs), and Pd-loaded porous  $\text{WO}_3$  NFs

synthesized by Pd-PS colloid templates (referred to as Pd-PS-WO<sub>3</sub> NFs) were demonstrated at highly humid ambient (90% RH) for potential application in breath analysis (Fig. 2). The dynamic response characteristic toward toluene was investigated at a concentration range of 0.1–5 ppm at 350 °C (Fig. 2a). A 4.5-fold and 7.6-fold improved response ( $R_{\text{air}}/R_{\text{gas}} = 12.1$  at 5 ppm) was observed with Pd-PS-WO<sub>3</sub> NFs compared to those of PS-WO<sub>3</sub> NFs ( $R_{\text{air}}/R_{\text{gas}} = 2.7$  at 5 ppm) and dense WO<sub>3</sub> NFs ( $R_{\text{air}}/R_{\text{gas}} = 1.6$  at 5 ppm). The measured minimum concentration of Pd-PS-WO<sub>3</sub> NFs was 100 ppb with a high response of 2.1 (Fig. 2a). The limit of detection capability toward toluene was investigated by exponential plotting based on the measured response values in the concentration range of 0.1–5 ppm. The result demonstrated that 50 ppb of toluene can be detected with a response of 1.5 (see ESI†, Fig. S4). The temperature-dependent response characteristic revealed that the improved toluene response properties were observed within a temperature range of 300–450 °C, exhibiting optimum sensing performance at 350 °C with a response of 12.1 at 5 ppm (Fig. 2b). In order to understand the improved response characteristics of PS-WO<sub>3</sub> NFs ( $R_{\text{air}}/R_{\text{gas}} = 2.7$  at 5 ppm) to toluene compared with those of the dense WO<sub>3</sub> NFs ( $R_{\text{air}}/R_{\text{gas}} = 1.6$  at 5 ppm), the nitrogen adsorption and desorption isotherms, Brunauer–Emmett–Teller (BET) surface areas, and Barrett–Joyner–Halenda (BJH) desorption average pore diameters were characterized (see ESI†, Fig. S5). The results revealed that the improved toluene response was attributed to the increased BET surface area (18.6 m<sup>2</sup> g<sup>−1</sup>) and average pore diameter (9 nm) of the PS-WO<sub>3</sub> NFs compared with the BET surface area (17 m<sup>2</sup> g<sup>−1</sup>) and average pore diameter (8.3 nm) of the dense WO<sub>3</sub> NFs. An important parameter to accomplish real-time breath analysis, response time was measured for Pd-PS-WO<sub>3</sub> NFs, which showed

very fast response times (<32 s) in a concentration range of 1–5 ppm compared to those (100–250 s) of dense WO<sub>3</sub> NFs and PS-WO<sub>3</sub> NFs (Fig. 2c). Multiple analyte detection characteristic of Pd-PS-WO<sub>3</sub> NFs was investigated with Pd-PS-WO<sub>3</sub> NFs at a gas concentration of 1 ppm with an operating temperature of 350 °C (Fig. 2d). High toluene response ( $R_{\text{air}}/R_{\text{gas}} = 5.4$  at 1 ppm) as well as comparable acetone response ( $R_{\text{air}}/R_{\text{gas}} = 5.1$  at 1 ppm) properties were confirmed with minor cross response characteristics ( $R_{\text{air}}/R_{\text{gas}} < 2.7$  at 1 ppm) toward other interfering analytes such as CO, ethanol, H<sub>2</sub>S, NO, pentane, and NH<sub>3</sub>.

The electrospinning method combined with the catalyst-decorated PS colloid templating route is highly advantageous considering that the sensing performances can be further optimized by controlling the concentration and density of catalyst-decorated PS colloid templates on SMO NFs. For example, increased content of Pd-PS colloid templates generated more pores and Pd functionalization on WO<sub>3</sub> NFs, which resulted in an enhanced toluene response ( $R_{\text{air}}/R_{\text{gas}} = 18.8$  at 5 ppm) as well as selectivity (see ESI†, Fig. S6). Furthermore, one would expect that diverse catalytic materials can be coated on the PS colloids using LbL assembly. To demonstrate the robustness of the catalyst-PS colloid templating route for exploring different types of catalyst-loaded porous SMO composite sensing layers, Pt-decorated PS colloid templates were prepared by simply changing the catalytic Pd precursor (K<sub>2</sub>PdCl<sub>4</sub>) into Pt precursor (K<sub>2</sub>PtCl<sub>4</sub>) and utilized in electrospinning to form Pt-loaded porous WO<sub>3</sub> NFs (hereafter, Pt-PS-WO<sub>3</sub> NFs) (see ESI†). Then, the different sensing performances were investigated using Pt-PS-WO<sub>3</sub> NFs compared with dense WO<sub>3</sub> NFs and PS-WO<sub>3</sub> NFs (Fig. 3). Catalytic Pt layers were successfully formed on the surface of PS colloid templates by LbL assembly (in the inset of Fig. 3a). In addition, Pt-PS-WO<sub>3</sub> NFs were obtained by introducing the synthesized Pt-decorated PS colloid templates in electrospinning followed by calcination at the same temperature (Fig. 3a). Similarly, closed and open pore structures (white arrows in Fig. 3a) were formed after decomposition of Pt-decorated PS colloid templates. EDS elemental mapping analysis using TEM revealed the well-distributed Pt functionalization at the pore sites of the porous WO<sub>3</sub> NFs (see ESI†, Fig. S3). The gas sensing measurement demonstrated that dramatically improved acetone sensing performance was observed with Pt-PS-WO<sub>3</sub> NFs, which was 43-fold and 52.4-fold higher response ( $R_{\text{air}}/R_{\text{gas}} = 120.5$  at 5 ppm) compared to those of PS-WO<sub>3</sub> NFs ( $R_{\text{air}}/R_{\text{gas}} = 2.8$  at 5 ppm) and dense WO<sub>3</sub> NFs ( $R_{\text{air}}/R_{\text{gas}} = 2.3$  at 5 ppm) at 350 °C (Fig. 3b).

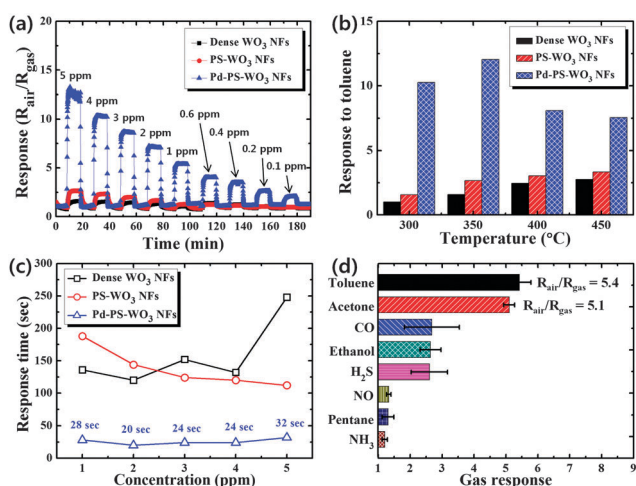


**Fig. 2** Toluene molecule sensing characteristics of dense WO<sub>3</sub> NFs, porous WO<sub>3</sub> NFs synthesized by PS colloid templates (PS-WO<sub>3</sub> NFs), and Pd-loaded porous WO<sub>3</sub> NFs (Pd-PS-WO<sub>3</sub> NFs) synthesized by Pd-decorated PS colloid templates: (a) dynamic toluene sensing transition in a concentration range of 0.1–5 ppm at 350 °C, (b) temperature-dependent toluene response characteristic at 5 ppm in a temperature range of 300–450 °C, (c) response time evaluation in a concentration range of 1–5 ppm at 350 °C, and (d) multiple analyte detection capability of Pd-PS-WO<sub>3</sub> NFs comparing the responses at a concentration of 1 ppm at 350 °C.

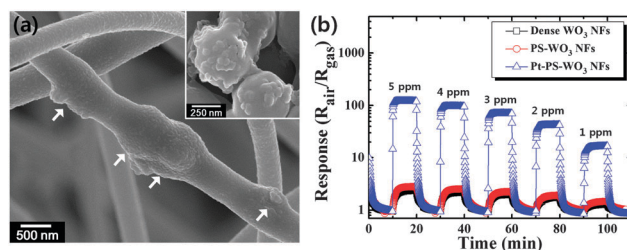


**Fig. 3** (a) SEM image of Pt-loaded porous WO<sub>3</sub> NFs (Pt-PS-WO<sub>3</sub> NFs) synthesized by Pt-decorated PS colloid templates (in the inset) and (b) dynamic acetone sensing transition of dense WO<sub>3</sub> NFs, PS-WO<sub>3</sub> NFs, and Pt-PS-WO<sub>3</sub> NFs in a concentration range of 1–5 ppm at 350 °C.



The highly acetone sensitive sensing layer of Pt-PS-WO<sub>3</sub> NFs can be applied for the monitoring of diabetes since the increased concentration (>1.8 ppm) of acetone is generated in the breath of the diabetics compared to the concentration (200–900 ppb) in the breath of healthy people.<sup>24</sup> The results envision that diverse catalysts can be decorated on the PS colloid templates and utilized as sacrificial templates to form multiple pores on the surface of SMO NFs simultaneously with the functionalization of catalytic materials at the pore sites, thereby optimizing the biomarker sensing performances for potential diagnostic application by breath analysis.

The mechanism of the improved toluene and acetone sensing performances of the catalyst-loaded WO<sub>3</sub> NFs was investigated. The basic sensing principle of SMOs is that resistivity changes are caused by the exposure of analyte molecules, which is attributed to the surface reaction between analyte molecules and chemisorbed oxygen species (*i.e.*, O<sup>−</sup>, O<sub>2</sub><sup>−</sup>, and O<sub>2</sub>). To further enhance the sensitivity and selectivity of the SMO-based sensors, noble metal catalysts were introduced into the SMO surface to induce the catalytic effect activating the surface reaction.<sup>25</sup> Generally, catalytic effects are categorized into chemical and electronic sensitization.<sup>26</sup> In the composite of Pd-PS-WO<sub>3</sub> NFs, catalytic Pd behaves as an electronic sensitizer by attracting and donating electrons in WO<sub>3</sub> NFs, which resulted in the modulation of a surface space charged layer. In other words, Pd can be oxidized to PdO (ref. 20) in air ambient by thickening the space charged layer at the surface of WO<sub>3</sub> NFs. PdO is then reduced to Pd by donating electrons back to the WO<sub>3</sub> NFs when reducing gases such as toluene and acetone are exposed to the sensor, which results in thinning of the space charged layer, thereby inducing large resistivity changes of the Pd-PS-WO<sub>3</sub> NF composite sensor. The catalytic effect of Pd on WO<sub>3</sub> NFs can activate surface reactions with the following reactions: C<sub>6</sub>H<sub>5</sub>CH<sub>3</sub> (gas) + 2O<sup>−</sup> → C<sub>6</sub>H<sub>5</sub>CH<sub>3</sub>O<sup>−</sup> + H<sub>2</sub>O + e<sup>−</sup> for toluene sensing<sup>27</sup> and CH<sub>3</sub>COCH<sub>3</sub> (gas) + O<sup>−</sup> → CH<sub>3</sub>COC<sup>+</sup>H<sub>2</sub> + OH<sup>−</sup> + e<sup>−</sup> or CH<sub>3</sub>COCH<sub>3</sub> (gas) + 2O<sup>−</sup> → C<sup>+</sup>H<sub>3</sub> + CO<sub>2</sub> + CH<sub>3</sub>O<sup>−</sup> + 2e<sup>−</sup> for acetone sensing,<sup>28</sup> which contribute to the improved selective sensing properties. In the case of the Pt-PS-WO<sub>3</sub> NF composite, a chemical sensitizer of Pt can activate dissociation of gas analytes and spill-over of the dissociated analytes to the surface of WO<sub>3</sub> NFs by facilitating a chemical reaction with the chemisorbed oxygen species. The origin of the resistivity changes in the chemical sensitization is, thus, related to the concentration of chemisorbed oxygen species on the surface of WO<sub>3</sub> NFs. Both electronic and chemical sensitizations are reported to enhance the gas response, selectivity, and response time properties,<sup>29</sup> which are also demonstrated in this work. We expect that further optimization of the catalyst loading amount on PS colloid templates can generate optimal sensing performances as a result of the catalytic sensitization effect and facile penetration of analytes through the pores.

In this work, a new catalyst functionalization method was successfully proposed *via* the electrospinning route using catalytic Pd- and Pt-decorated PS colloid templates, particularly for the synthesis of Pd- and Pt-loaded porous WO<sub>3</sub> NFs. Catalyst-decorated PS colloid templates were prepared by well-established LbL assembly. Highly porous nanofibrous WO<sub>3</sub> structure simultaneously with catalyst decoration at the pore sites was achieved by the catalyst-decorated PS colloid templating route during electrospinning.

As a result, catalytic Pd- and Pt-loaded porous WO<sub>3</sub> NFs exhibited dramatically improved toluene ( $R_{\text{air}}/R_{\text{gas}} = 12.1$  at 5 ppm) and acetone ( $R_{\text{air}}/R_{\text{gas}} = 120.5$  at 5 ppm) sensing performances. The proposed LbL-assisted catalyst assembled templates are promising to develop diverse catalyst-porous SMO composite sensor arrays for highly sensitive and selective sensing of biomarker molecules in breath for diagnostic applications.

This work was supported by the Center for Integrated Smart Sensors funded by the Ministry of Science, ICT & Future Planning as Global Frontier Project (CISS-2011-0031870) and Korea Advanced Institute of Science and Technology (KAIST) funded by the Ministry of Science, ICT & Future Planning as End Run Project (N01140506).

## Notes and references

- 1 M. Phillips, K. Gleeson, J. M. B. Hughes, J. Greenberg, R. N. Cataneo, L. Baker and W. P. McVay, *Lancet*, 1999, **353**, 1930–1933.
- 2 G. Peng, U. Tisch, O. Adams, M. Hakim, N. Shehata, Y. Y. Broza, S. Billan, R. Abdah-Bortnyak, A. Kuten and H. Haick, *Nat. Nanotechnol.*, 2009, **4**, 669–673.
- 3 M. Righettoni, A. Tricoli and S. E. Pratsinis, *Anal. Chem.*, 2010, **82**, 3581–3587.
- 4 P. Montuschi, S. A. Kharitonov and P. J. Barnes, *Chest*, 2001, **120**, 496–501.
- 5 E. Tseliou, V. Bessa, G. Hillas, V. Delimpoura, G. Papadaki, C. Roussos, S. Papiris, P. Bakakos and S. Loukides, *Chest*, 2010, **138**, 107–113.
- 6 S. J. Choi, B. H. Jang, S. J. Lee, B. K. Min, A. Rothschild and I. D. Kim, *ACS Appl. Mater. Interfaces*, 2014, **6**, 2588–2597.
- 7 I. Lee, S. J. Choi, K. M. Park, S. S. Lee, S. Choi, I. D. Kim and C. O. Park, *Sens. Actuators, B*, 2014, **197**, 300–307.
- 8 O. Barash, N. Peled, F. R. Hirsch and H. Haick, *Small*, 2009, **5**, 2618–2624.
- 9 H. Haick, Y. Y. Broza, P. Mochalski, V. Ruzsanyi and A. Amann, *Chem. Soc. Rev.*, 2014, **43**, 1423–1449.
- 10 M. Righettoni, A. Amann and S. E. Pratsinis, *Mater. Today*, 2014, DOI: 10.1016/j.mattod.2014.08.017.
- 11 S. J. Choi, M. P. Kim, S. J. Lee, B. J. Kim and I. D. Kim, *Nanoscale*, 2014, **6**, 11898–11903.
- 12 M. Righettoni, A. Tricoli, S. Gass, A. Schmid, A. Amann and S. E. Pratsinis, *Anal. Chim. Acta*, 2012, **738**, 69–75.
- 13 S. J. Choi, F. Fuchs, R. Demadrille, B. Grevin, B. H. Jang, S. J. Lee, J. H. Lee, H. L. Tuller and I. D. Kim, *ACS Appl. Mater. Interfaces*, 2014, **6**, 9061–9070.
- 14 A. Greiner and J. H. Wendorff, *Angew. Chem., Int. Ed.*, 2007, **46**, 5670–5703.
- 15 C. L. Zhang and S. H. Yu, *Chem. Soc. Rev.*, 2014, **43**, 4423–4448.
- 16 N. G. Cho, H. S. Woo, J. H. Lee and I. D. Kim, *Chem. Commun.*, 2011, **47**, 11300–11302.
- 17 S. H. Choi, G. Ankonina, D. Y. Youn, S. G. Oh, J. M. Hong, A. Rothschild and I. D. Kim, *ACS Nano*, 2009, **3**, 2623–2631.
- 18 J. Shin, S. J. Choi, I. Lee, D. Y. Youn, C. O. Park, J. H. Lee, H. L. Tuller and I. D. Kim, *Adv. Funct. Mater.*, 2013, **23**, 2357–2367.
- 19 D. J. Yang, I. Kamiyenchick, D. Y. Youn, A. Rothschild and I. D. Kim, *Adv. Funct. Mater.*, 2010, **20**, 4258–4264.
- 20 N. H. Kim, S. J. Choi, D. J. Yang, J. Bae, J. Park and I. D. Kim, *Sens. Actuators, B*, 2014, **193**, 574–581.
- 21 F. Caruso, R. A. Caruso and H. Mohwald, *Science*, 1998, **282**, 1111–1114.
- 22 Y. Wang, A. S. Angelatos and F. Caruso, *Chem. Mater.*, 2008, **20**, 848–858.
- 23 K. Suematsu, Y. Shin, Z. Q. Hua, K. Yoshida, M. Yuasa, T. Kida and K. Shimanoe, *ACS Appl. Mater. Interfaces*, 2014, **6**, 5319–5326.
- 24 S. J. Choi, I. Lee, B. H. Jang, D. Y. Youn, W. H. Ryu, C. O. Park and I. D. Kim, *Anal. Chem.*, 2013, **85**, 1792–1796.
- 25 I. D. Kim, A. Rothschild and H. L. Tuller, *Acta Mater.*, 2013, **61**, 974–1000.
- 26 N. Yamazoe, G. Sakai and K. Shimanoe, *Catal. Surv. Asia*, 2003, **7**, 63–75.
- 27 X. H. Ding, D. W. Zeng, S. P. Zhang and C. S. Xie, *Sens. Actuators, B*, 2011, **155**, 86–92.
- 28 R. S. Khadayate, V. Sali and P. P. Patil, *Talanta*, 2007, **72**, 1077–1081.
- 29 N. Yamazoe, *Sens. Actuators, B*, 1991, **5**, 7–19.